Chemical
Science

ROYAL SOCIETY
OF CHEMISTRY

EDGE ARTICLE

View Article Online
View Journal | View Issue

Check for updates

Cite this: *Chem. Sci.*, 2023, **14**, 11554

All publication charges for this article have been paid for by the Royal Society of Chemistry

Received 21st June 2023
Accepted 1st October 2023

DOI: 10.1039/d3sc03153e

rsc.li/chemical-science

Multiexciton quintet state populations in a rigid pyrene-bridged parallel tetracene dimer†

Liang-Chun Lin,[a] Tanner Smith,[b] Qianxiang Ai,[b] Brandon K. Rugg,[c] Chad Risko,[b] John E. Anthony,[b] Niels H. Damrauer[ad] and Justin C. Johnson[*cd]

The multiexciton quintet state, ^{5}TT, generated as a singlet fission intermediate in pairs of molecular chromophores, is a promising candidate as a qubit or qudit in future quantum information science schemes. In this work, we synthesize a pyrene-bridged parallel tetracene dimer, **TPT**, with an optimized interchromophore coupling strength to prevent the dissociation of ^{5}TT to two decorrelated triplet (T_1) states, which would contaminate the spin-state mixture. Long-lived and strongly spin-polarized pure ^{5}TT state population is observed *via* transient absorption spectroscopy and transient/pulsed electron paramagnetic resonance spectroscopy, and its lifetime is estimated to be >35 μs, with the dephasing time (T_2) for the ^{5}TT-based qubit measured to be 726 ns at 10 K. Direct relaxation from ^{1}TT to the ground state does diminish the overall excited state population, but the exclusive ^{5}TT population at large enough persistent density for pulsed echo determination of spin coherence time is consistent with recent theoretical models that predict such behavior for strict parallel chromophore alignment and large exchange coupling.

Introduction

Singlet fission (SF) is a process in which the photoexcited singlet (S_1) transforms into two low-energy triplets (T_1), and it has been widely investigated to improve the photovoltaic conversion efficiency.[1–5] The singlet-coupled triplet pair, ^{1}TT, is a spin-entangled biexciton state that forms in every SF reaction *via* internal conversion from S_1. For the past decade or so, researchers have been focusing on generating maximum decorrelated T_1 through ^{1}TT for solar cell applications.[4,6] Here, in contrast, we prevent ^{1}TT from decaying to T_1 and drive the intersystem crossing from ^{1}TT to ^{5}TT manifolds in a highly state-selective fashion for quantum information science (QIS) applications by designing and synthesizing a parallel rigid organic dimer. The SF-born ^{5}TT manifold is regarded as a novel platform to make a quantum bit, or qubit, due to its strong spin polarization *via* optical excitation and the ability to perform fast quantum gate operations with microwave pulses.[7] As an $S = 2$ manifold, it also has the potential to operate in a qudit scheme. Furthermore, results from time-resolved electron paramagnetic resonance spectroscopy (TREPR), and pulsed EPR in both monomer thin films[8–11] and organic dimers[12–16] have verified ^{5}TT formation and laid the groundwork for understanding the spin evolution.

Considering the angular momentum coupling between the triplets in (TT) states, nine possible (TT) states can be constructed, including ^{1}TT (one spin sublevel), ^{3}TT (three spin sublevels) and ^{5}TT (five spin sublevels). The state selectivity from ^{1}TT to ^{5}TT requires symmetry of the spin-exciton Hamiltonian, $H = JS_A{\cdot}S_B + H_A + H_B$, where J represents isotropic exchange energy between the spin on each chromophore, and $H_{A,B}$ are the anisotropic terms for dipolar interaction within chromophore A and B, $H_i = D\left(S_{iz}{}^2 - \frac{S_i{}^2}{3}\right)$, i = A, B. The fine–structure interaction, governing the interconversion between the nine states, perturbs the spin-exciton Hamiltonian and makes the eigenstates of the Hamiltonian not $^{2S+1}\mathrm{TT}_{M\ (-S\le M\le S)}$ states but the combination of them. However, under conditions of large J, these interactions are typically negligible. The parallel JDE model[7] of the spin-exciton Hamiltonian assumes the two chromophores to be identical and parallel to share the same coordinate axis. Under these conditions, the conversion from ^{1}TT to ^{5}TT while isolating ^{3}TT is guaranteed by the Hamiltonian symmetry. Also, based on the parallel JDE model selection rules only the transition from ^{1}TT to $^5\mathrm{TT}_0$ ($m_s = 0$) and $^5\mathrm{TT}_{\pm2}$ ($m_s = \pm2$) are allowed when the external magnetic axis and the molecular axis are aligned. Further, the relative kinetics of the $^1\mathrm{TT} \rightarrow {}^5\mathrm{TT}_0$ and $^5\mathrm{TT}_{\pm2}$ transitions are proportional to the zero-field parameters D^2 and E^2, respectively, leaving the $^5\mathrm{TT}_0$

---

[a] Department of Chemistry, University of Colorado Boulder, Boulder, CO 80309, USA

[b] Department of Chemistry & Center for Applied Energy Research, University of Kentucky, Lexington, Kentucky 40506-0055, USA

[c] National Renewable Energy Laboratory, 15013 Denver West Parkway, Golden, Colorado 80401, USA. E-mail: justin.johnson@nrel.gov

[d] Renewable and Sustainable Energy Institute (RASEI), University of Colorado Boulder, Boulder, CO, 80309, USA

† Electronic supplementary information (ESI) available: Synthesis details and characterization, additional steady-state and transient optical and EPR spectroscopy, TDDFT and exchange energy calculations, details of the kinetic models and associated fits. See DOI: **https://doi.org/10.1039/d3sc03153e**

pathway as dominant because $D \geq 3E$ by definition. All accessible dimer geometries must be included in this analysis, and for flexible systems, particularly about the bridge, significant conformational diversity can result. This motivates the use of both chromophore and bridge with limited flexibility to simplify the spin evolution pathways.

In this work, the rigid parallel organic dimer consists of two silylacetylene-substituted tetracene chromophores bridged with pyrene, **TPT**, and the structure can be seen in Fig. 2b. A similar dimer, APA, where two silylacetylene-substituted anthracenes are bridged with pyrene, has previously been characterized with UV-Vis and computational chemistry analysis.[17] Electronic coupling between the two chromophores is weak, yet the interaction between the anthracenic moiety and the pyrene bridge is strong, making the S_1 energy of the chromophore to be between that of silylacetylene-substituted anthracene and tetracene. For **TPT**, the properties of the tetracene moiety can also be tuned by the pyrene bridge to mimic a combination of silylacetylene-substituted tetracene and pentacene. We will demonstrate that the mixed nature of the chromophore excited state facilitates the formation and preservation of ^{5}TT. This stands in contrast to other flexible-bridged pentacenic dimer systems wherein independent triplets are the primary long-lived product (whether directly from ^{5}TT or *via* intersystem crossing from ^{3}TT), rather than ^{5}TT as the surviving species.[13,14,18,19] Another rigid-bridged pentacene dimer was recently reported to almost exclusively form ^{5}TT$_0$, but the apparent yield was low.[12] Our results reveal the first non-pentacene dimer to form a high yield of exclusively ^{5}TT that persists to μs.

Results

Synthesis of TPT

Shown in Fig. 1 and S1,† the synthetic routes to **TPT** and **PT** involve intermediates **1** and **3**, which have previously been reported.[17] Reaction of **1** with 1,4-anthraquinone and KI yields the pyrenebis(tetracenequinone) **2**. The addition of lithiated *n*-octyldiisopropylsilyl (NODIPS) acetylene followed by the addition of tin(II) chloride in aqueous HCl gives **TPT**. The synthesis of **PT** likewise consisted of the addition of 1,4-anthraquinone to **3** to yield pyrene-tetracenequinone **4**, followed by addition of lithiated NODIPS-acetylene. Removal of Br from the diol intermediate **5** was initially attempted using a Pd catalyst at 100 °C, however these conditions resulted in apparent decomposition of the starting material and none of the target product was recovered. Debromination of **5** was ultimately achieved through metal–halogen exchange at low temperature, and subsequent addition of aq. HCl and tin(II) chloride to yield the aromatized product **PT**.

Optical spectra and origin of transitions

Fig. 2a shows molar extinction spectra for **PT** and **TPT**. To the red, the vibronic peaks ranging from 500 nm to 625 nm are attributed to the short axis polarized $S_1 \leftarrow S_0$ transition of the tetracene moieties. The peak for the $S_1 \leftarrow S_0$ 0–0 vibronic transition of **PT** is centered at 603 nm, located in between that of TIPS-tetracene and TIPS-pentacene,[20,21] measured to be at 530 nm and 638 nm, respectively. The ~70 nm redshift from TIPS-tetracene and ~40 nm blueshift from TIPS-pentacene for **PT** (0.28 eV and 0.11 eV, respectively)[20] result from the limited extension of the acene system.[17] Comparing **PT** and **TPT**, as seen in Fig. 2a, for the $S_1 \leftarrow S_0$ transition, **TPT** has extinction coefficient ~2 times that of **PT**. The fact that the extinction coefficient of a dimer is 2 times of the monomer suggests that the **TPT** is in a weakly coupled regime in terms of the interaction between the two chromophore units. This is further substantiated by the only ~2 nm redshift for 0–0 transition from **PT** to **TPT**. Furthermore, the ratio of 0–0 to 0–1 absorption/emission intensity (I_{0-1}/I_{0-0}) for TPT and PT are both ~1.4 as can be seen in Fig. S7.† However, for the long-axis $S_3 \leftarrow S_0$ transition of

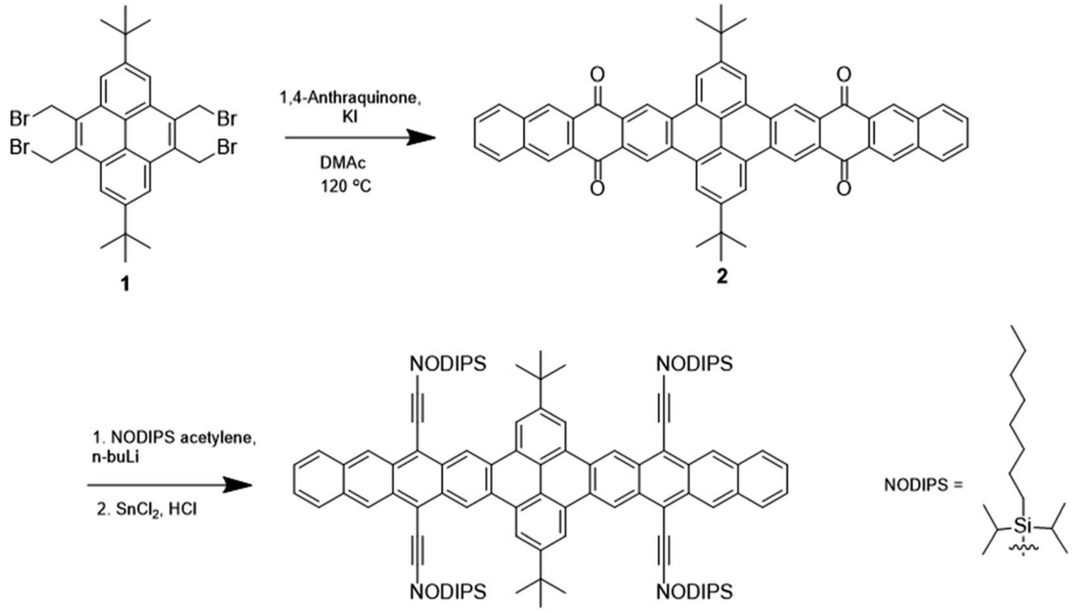

Fig. 1 Synthetic scheme for TPT.

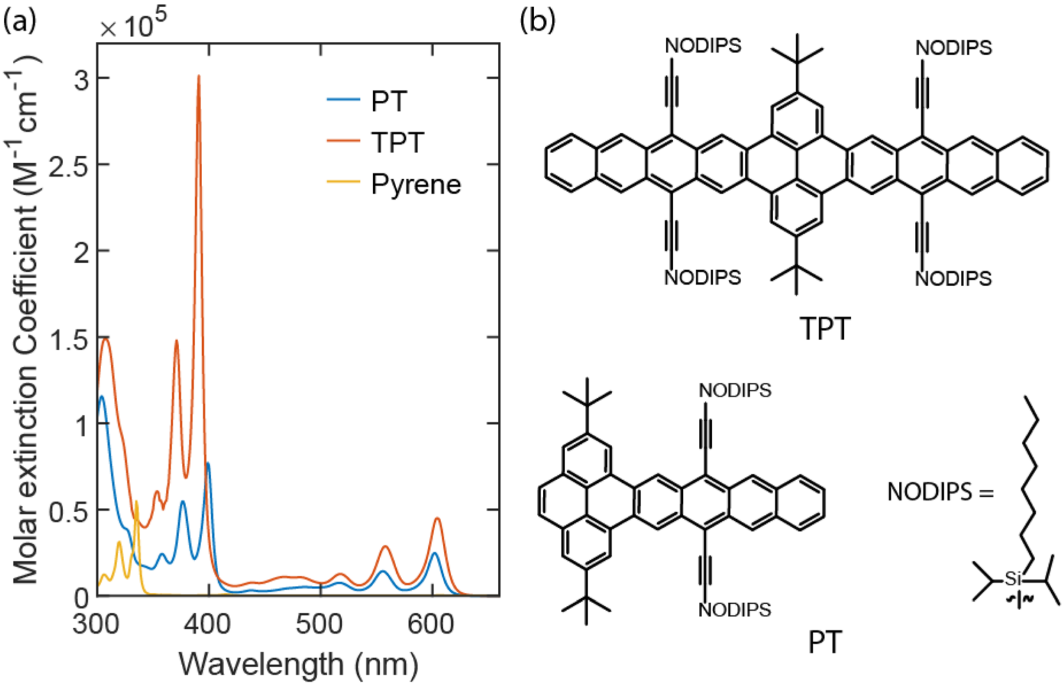

Fig. 2 Molar extinction spectra for both **PT** (blue line) and **TPT** (red line) in toluene. The molar extinction spectrum for pyrene in cyclohexane is in yellow.

the chromophores around 315 nm, the extinction coefficient of **TPT** is less than two times of **PT**, suggesting some perturbation of higher-lying excited states. The extinction coefficient of the expected pyrene peaks in **TPT** is enhanced by roughly 5 times from the pyrene itself and from **PT**.

The vibronic peaks for **PT** and **TPT** within the 350 nm to 425 nm window, as indicated by TDDFT calculations, originate from a singlet excitation with contributions from both pyrene and tetracene segments. In **PT**, this excitation has two similarly weighted natural transition orbital (NTO) pairs that, as shown in Fig. S5a,† resemble tetracene HOMO → pyrene LUMO and pyrene HOMO → tetracene LUMO, respectively. As a result, the net charge transfer from pyrene to tetracene, compared to charge redistribution within these fragments, is negligible. This is confirmed by the two-fragment charge transfer matrix (Fig. S5b†) in which off-diagonal (diagonal) elements represent inter-fragment charge transfer (charge redistribution). The transition densities of this excitation are shown in Fig. S5c† with a transition dipole moment of 3.82 a.u. polarized along the long-axis (the directions along which the transition density switches its sign). This is in contrast to the vibronic peaks from 500 nm to 625 nm ($S_1 \leftarrow S_0$) that result from the local excitation of tetracene with a transition dipole moment polarized along the short-axis.[15]

Similar to **PT**, the excitation responsible for vibronic peaks from 350 nm to 425 nm in **TPT** is polarized along the long axis (Fig. S5f†). The NTOs (Fig. S5d†) also largely resemble frontier molecular orbitals of pyrene and tetracene, featuring bidirectional charge transfer from the pyrene segment to both tetracene segments. This is corroborated by the three-fragment charge transfer matrix (Fig. S5e†) in which one-direction charge transfer contributions between pyrene and tetracene fragments largely cancel each other, resulting in a small net charge transfer from pyrene to tetracene fragments. The addition of another tetracene segment leads to an increased transition dipole moment of 7.80 a.u. for this excitation, approximately double of that in **PT**. This is in good agreement with the experimentally observed extinction coefficient ratio (4 : 1) between **TPT** and **PT**.

The associated peaks for pyrene in cyclohexane[22] are measured to be from 300 nm to 350 nm. The peak centered ~315 nm for **PT** and **TPT** corresponds to the $S_3 \leftarrow S_0$ transition of the tetracene moieties. NTOs of this excitation of **PT** are shown in Fig. S6a.† The two equally weighted NTO pairs resemble pentacene HOMO−2 → pentacene LUMO and pentacene HOMO → pentacene LUMO+2, respectively, as the extension of the acene system with the pyrene bridge mimics a pentacene unit. This is primarily a local excitation at the acene fragment, as indicated by the large diagonal element in its fragment charge transfer matrix (Fig. S6b†), with moderate bidirectional charge transfer yielding a small net charge transfer from tetracene to pyrene. Fig. S6c† shows the transition densities with a dipole moment of 4.45 a.u. along the long axis. Both NTOs and transition densities are similar to that of the ^1B_b state of pentacene.[23]

The situation is more complicated for **TPT**. As shown in Fig. S6d,† another NTO pair (the third one), resembling pyrene HOMO → tetracene LUMO, appears with non-negligible contributions. Similar contributions were made to the hole and electron densities from the three fragments, leading to small differences among elements in the fragment charge transfer matrix (Fig.S6e†). Unlike the case in the previous section, where transition densities of **TPT** are roughly that of **PT** duplicated by a mirror plane along the 2, 7 positions of pyrene, transition densities of this excitation (Fig. S6f†) cannot be produced as such, likely due to the aforementioned additional NTO pair. The transition dipole moment is calculated to be 4.20 a.u. which is similar to that of **PT**, agreeing with the similar extinction coefficients for **PT** and **TPT** observed experimentally.

Davydov splitting, caused by interchromophore interaction of transition dipoles in a singlet fission dimer, should also be mentioned, especially for the rigidly bridged dimer. Davydov splitting for both $S_1 \leftarrow S_0$ and $S_3 \leftarrow S_0$ transitions have been observed from both norbornyl-bridged tetracene and pentacene

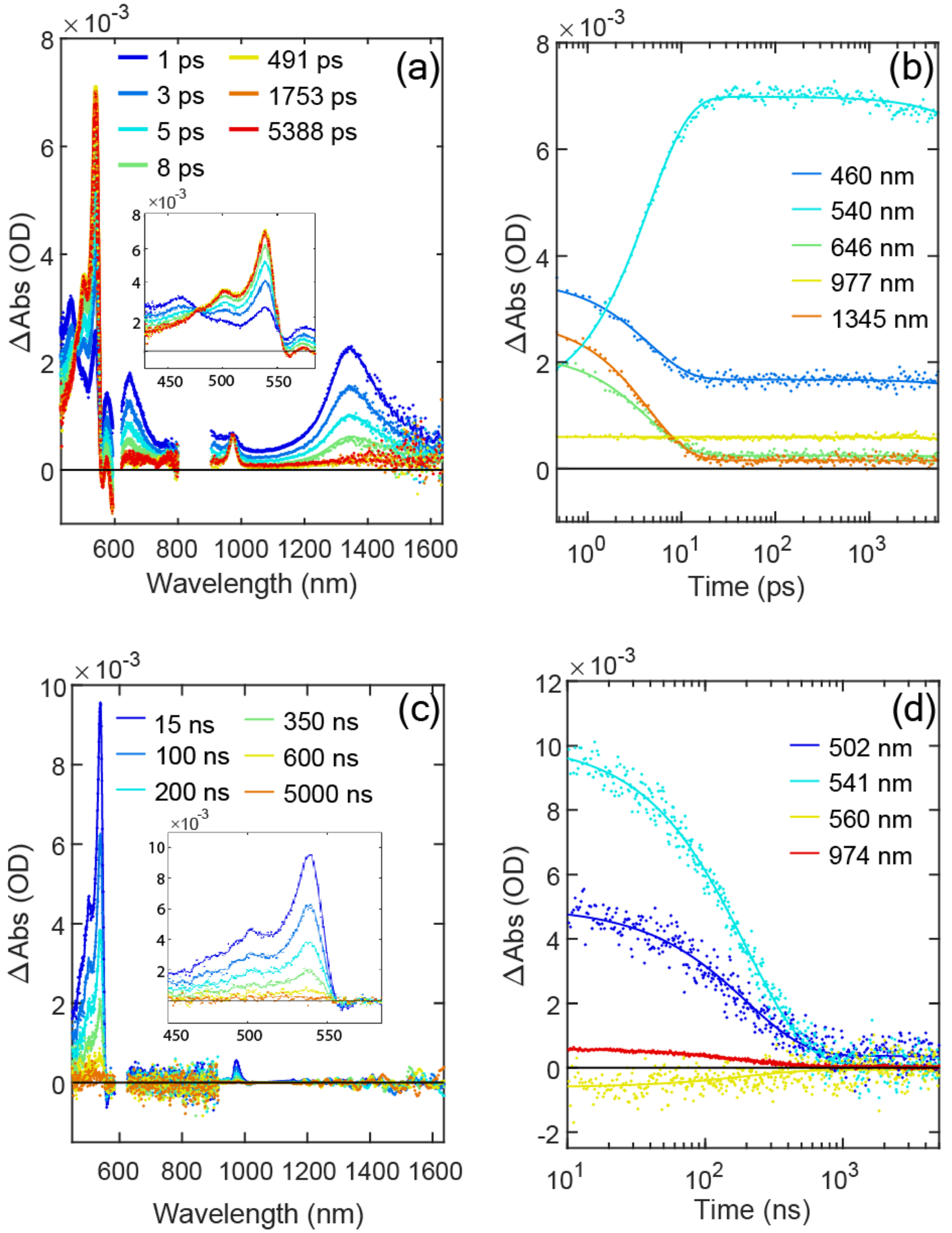

Fig. 3 (a) Spectra at selected delay times for fsTA of **TPT** in 2-MeTHF at room temperature. Dots represent the raw data, and the solid lines represent the fit. (Inset) Spectra in visible region only. (b) Kinetic traces at selected wavelengths from (a). (c) Spectra at selected delay times for nsTA of **TPT** in 2-MeTHF at room temperature. (Inset) Spectra in visible region only. (d) Kinetic traces at selected wavelengths from (c).

dimers.[20,21] For **TPT**, the two tetracene chromophores are held firmly at 180° from each other to form a planar dimer. Due to the flat structure of the molecule and the parallel nature of the two tetracene chromophores, the Davydov splitting for long-axis ($S_3 \leftarrow S_0$) and short-axis ($S_1 \leftarrow S_0$) transitions are not observed in Fig. 2a.

Photoluminescence

In Fig. S7 and S8,† $S_0 \leftarrow S_1$ 0–0 emission peaks for **TPT** and **PT** are found to be 2.04 eV and 2.05 eV, respectively. Similar S_1 energies for dimer and monomer suggests minimal electronic delocalization between the two tetracenic chromophores for **TPT**. However, the emission quantum yield $\Phi_{\text{emi}}$for **TPT** is significantly smaller than **PT**, measured to be 6% and 100%, respectively. Photoluminescence kinetics for **PT**, obtained *via* time-correlated single photon counting (TCSPC), are displayed in Fig. S9b.† The relationship between Φ_{emi} and the kinetics of S_1 can be described with the formula: $\Phi_{\text{emi}} = \dfrac{k_{\text{r}}}{k_{\text{r}} + k_{\text{nr}}}$, where k_{r} and k_{nr} represent radiative and nonradiative S_1 decay coefficient, respectively. We obtain $1/k_{\text{r}}$ to be 23 ± 0.02 ns from fitting the TCSPC measurement to a single exponential decay under conditions where Φ_{emi} is 100%. We show that $1/(k_{\text{r}} + k_{\text{nr}})$ is 22.6 ± 0.2 ns from TA (*vida infra*) in Fig. S10a and b,† consistent with the measured Φ_{emi} of 100%. For TCSPC traces of **TPT**, shown in Fig. S9c and d,† we can see an early decay from the fast fission process and a slow decay with a lifetime fitted to be 21.2 ± 0.02 ns, which is similar to the S_1 lifetime from **PT** (Fig. S9a and b†). We assign the low emission quantum yield of **TPT** as due to the efficient singlet fission process, which will be verified below.

Femtosecond transient absorption (fsTA). **TPT** is excited by a ∼100 fs optical pulse centered at 600 nm, where the $S_1 \leftarrow S_0$ 0–0 transition is located. As shown in Fig. 3a, the transient absorption spectrum evolves from the earliest species (S_1, delay time = 1 ps in blue) to the later species (putative ^{1}TT, delay time = 5388 ps in red) in 2-MeTHF at room temperature. An excited state absorption (ESA) feature of the S_1 state (blue) rises immediately upon excitation from S_0 to S_1, and it appears in both visible (VIS) and near-IR (NIR) regions. In the VIS region, S_1 ESA consists of a broad band from 430 nm to 550 nm with relatively sharp peaks at 462 nm and 539 nm, corresponding to the $S_n \leftarrow S_1$ transition. A dip centered at 560 nm is associated with the ground state bleach ($S_0 \leftarrow S_1$). The other band centered at 648 nm from 600 nm to 800 nm is assignable to a $S_5 \leftarrow S_1$ transition. In the NIR region, a weak band from 900 nm to 1000 nm is from the $S_4 \leftarrow S_1$ transition, and a larger peak centered at 1345 nm is attributed to the $S_3 \leftarrow S_1$ transition.[24] The decay of the S_1 features can be seen in Fig. 3b. At 460 nm, the S_1 state decays to an offset within ∼ 10 ps, and kinetics at both 646 nm and 1339 nm show a similar decay as at 460 nm, suggesting they all originate from the S_1 state. While the S_1 state decays, it evolves to ^{1}TT, and two isosbestic points at 478 nm and 553 nm indicate direct conversion between these species. In the visible region, a characteristic triplet ESA with a main peak at 539 nm and a shoulder peak at 502 nm appears, which we relate to $\text{TT}_n \leftarrow \text{TT}_1$. A kinetically correlated band between 600 nm and 800 nm can also be assigned to the $\text{TT}_n \leftarrow \text{TT}_1$ transition, and another relatively sharp triplet peak centered at 974 nm is found that has been previously verified as a signature of the triplet state.[25] As depicted in Fig. 3b, the decay of the S_1 state gives rise to the ^{1}TT state completely within about 10 ps, which can be most clearly followed as a rise at 540 nm. The biexciton formation time is extracted from the global fit of the biexponential function to be 4.5 ± 0.02 ps. In contrast, no triplet-like features are found in TA for **PT**, Fig. S10.†

Applying the (A → B → 0) model based on the biexponential fitting result, we determined the species associated spectra (SAS) for S_1 and ^{1}TT, which can be seen in Fig. S11.† The S_1 ESA from TPT shows a similar spectral shape compared to the S_1 ESA from **PT**. In Fig. S11a† the redshift from S_1(**TPT**) to S_1(**PT**) at ∼465 nm and ∼1350 nm is apparent, suggesting S_n delocalization is facilitated by the bridge, to be discussed further below. Turning to the triplet, the spectral shape of the ^{1}TT ESA features approximately aligns with those of the T_1 measured through anthracene sensitization, as shown in Fig. S11b and S15.† However, a blueshift in the visible peak and a redshift in the NIR region (974 nm → 987 nm) is apparent from ^{1}TT to T_1.

At 77 K, the biexciton formation time increases to 8.3 ± 0.1 ps (Fig. S12†). The spectral shape of the triplet shows only a minor redshift at 77 K compared to room temperature, shown in Fig. 4a. The slowing of the fission process at 77 K suggests that singlet fission of **TPT** is thermally activated; selected kinetic traces for both temperatures in VIS and NIR regions are shown in Fig. S13a and b.† As a thermally activated yet reversible singlet fission process, the equilibrium between S_1 and ^{1}TT is also temperature dependent. The S_1 ESA remaining on ns timescales in the normalized fsTA time trace at room temperature and at 77 K (1345 nm and 1356 nm in Fig. 3b and S12b,† respectively) are measured to be ∼0.065 and ∼0.042, respectively, which are the signal portions relative to maximum S_1 signal at early times. The 6.5% remaining S_1 ESA amplitude is consistent with the emission quantum yield measurement mentioned above (∼6%).

Nanosecond transient absorption (nsTA). In Fig. 3c and d, we show the remaining species after 5 ns, ^{1}TT, which decays on a ns–μs timescale at room temperature. However, ^{1}TT does not decay completely to S_0 – a small but non-negligible offset remains in the visible region at later time. Considering the long-lasting unknown species, fitting the nsTA spectra with a single exponential function is not sufficient. Here, we fit the nsTA data globally with a bi-exponential function, $A_{^1\text{TT}}(\lambda)\exp\left(-\dfrac{t}{\tau_{^1\text{TT}}}\right) + A_{\text{X}}(\lambda)\exp\left(-\dfrac{t}{\tau_{\text{X}}}\right)$, to represent both ^{1}TT and the other species initially labeled X. In Fig. 3c, the characteristic triplet peak at 540 nm and the shoulder at 502 nm decay to the long-lasting X, with peaks at ∼520 nm and a shoulder at ∼556 nm. $\tau_{1_{\text{TT}}}$ obtained from the global fit is 197.4 ± 1.5 ns. However, τ_{X} from the fit is inaccurate due to the relatively small signal, which is <5% of ^{1}TT. Therefore, we report only the lower limit of τ_{X} to be ∼35 μs. While a lower limit, the lifetime is markedly below that determined for T_1 using sensitization experiments where we observe >150 μs. At 77 K, the ^{1}TT ESA

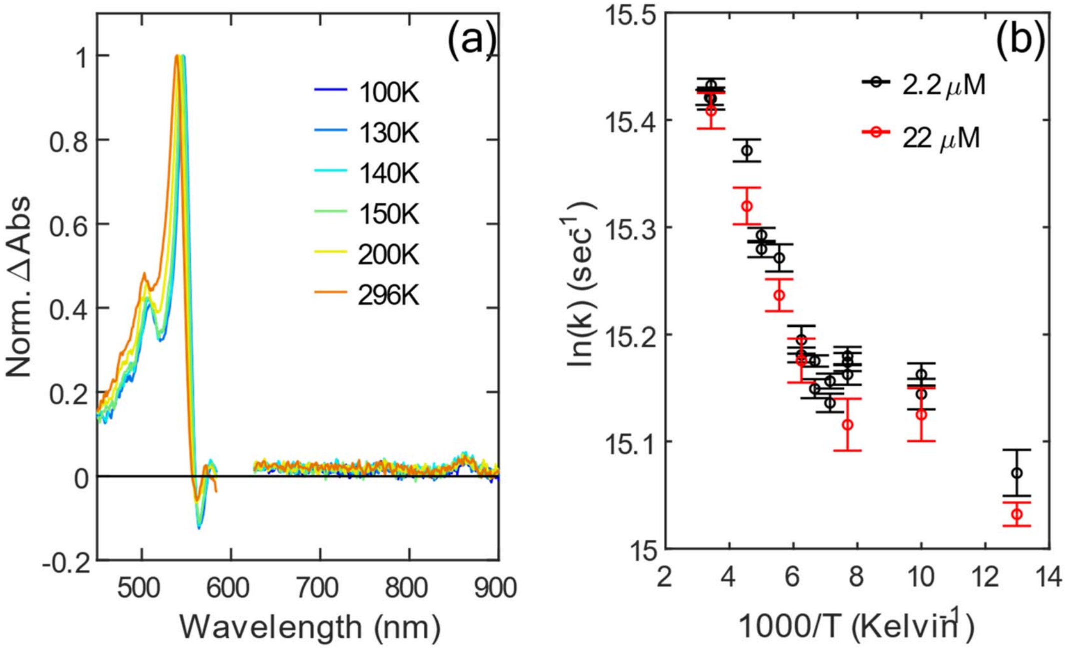

Fig. 4 (a) Normalized ^{1}TT spectra at different temperatures. (b) Arrhenius plot for the ^{1}TT decay rate coefficient at two different concentrations.

shows similar spectral features as the ESA in room temperature, except with a ∼10 nm redshift. The X ESA observed at room temperature can also be seen in the later time at 77 K in Fig. S12c.† Therefore, we again fit the nsTA at 77 K with the bi-exponential function. The $\tau_{1_{TT}}$ extracted from the global fit is 286.2 ± 5.3 ns, which is longer than 197 ns measured at room temperature.

We now turn to the temperature dependent kinetics of ^{1}TT and X based on the biexponential fit introduced above. From the global fit of nsTA, we normalize the ESA of ^{1}TT to the maximum of the triplet peak, which is shown in Fig. 4a. The triplet feature redshifts by 10 nm from 296 K to 77 K. Fig. 4b is the Arrhenius plot for the decay rate coefficient of ^{1}TT, $1/\tau_{1_{TT}}$, measured at two different concentrations: 2.2 μM and 22 μM. The agreement between $\tau_{1_{TT}}$ and the nearly constant spectral shapes at the two concentrations (*cf.*, Fig. S17 and S18† for concentration and temperature dependence) indicates that the environment for molecules in the solutions is similar, and that

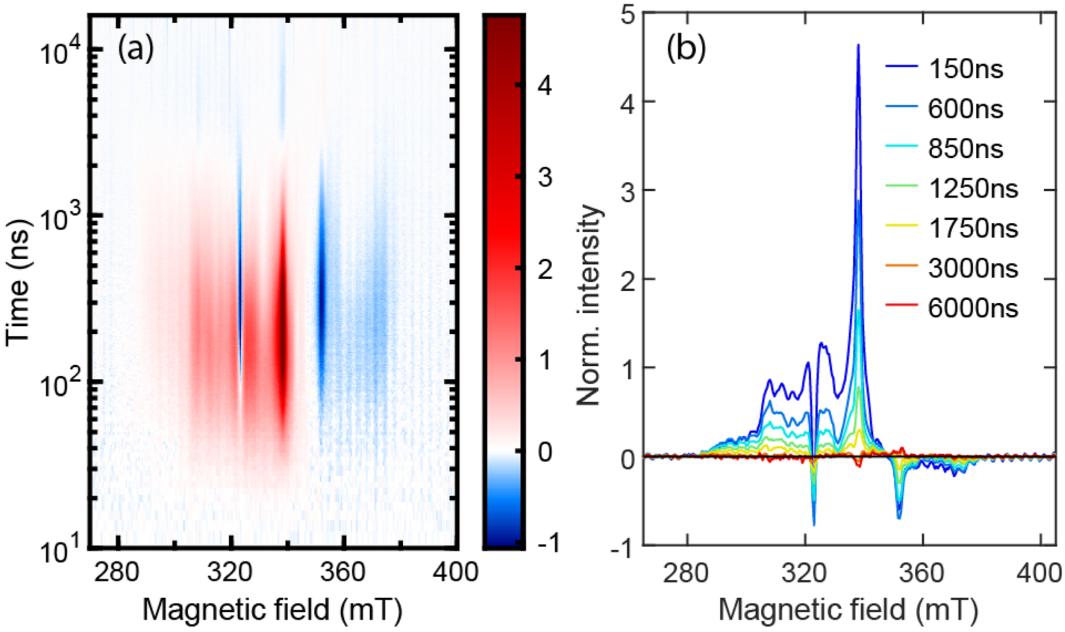

Fig. 5 (a) Normalized TREPR 2D plot for **TPT** in 2-MeTHF at 77 K. (b) Normalized EPR spectra from (a) at the selected delay times.

aggregation is not playing a significant role in the photophysics. However, the data from 130 K to 77 K show a stark change in slope compared with temperatures higher than 130 K, indicating a violation of the expected Arrhenius trend. The change occurs very near the glass transition of 2-MeTHF at ~137 K. Despite this abrupt change in temperature-dependent decay kinetics of ^{1}TT, the spectral amplitude of the long-lived X does not show much temperature dependence from 77 K to 296 K, as seen in Fig. S14b.†

Electron paramagnetic resonance (EPR). We directly measured the spin-active species *via* TREPR upon exciting the frozen **TPT**/2-MeTHF solution with a pulse centered at 600 nm as shown in Fig. 5. In Fig. 5a, the X-band EPR signal ranges from 280 mT to 380 mT, and it shows a spin polarization pattern of aeaae. The triplet EPR spectrum obtained by optically exciting **PT** in heavy-atom solvent at 76 K is shown in Fig. S16.† There the separation between the emissive and absorption peaks suggests D, the zero-field splitting parameter, to be 1260 MHz. In Fig. 5a, the separation between the inner peaks at 325 mT and 340 mT is 420 MHz, which is $D/3$, indicating the two peaks represents transitions between $m_s = \pm 1$ and $m_s = 0$ in ^{5}TT.[11] There are outer peaks at ~310 mT and ~355 mT, and the split is equal to D. Thus, these peaks could be related to the transitions between $m_s = \pm 1$ and $m_s = 0$ in the T_1 manifold or transitions between

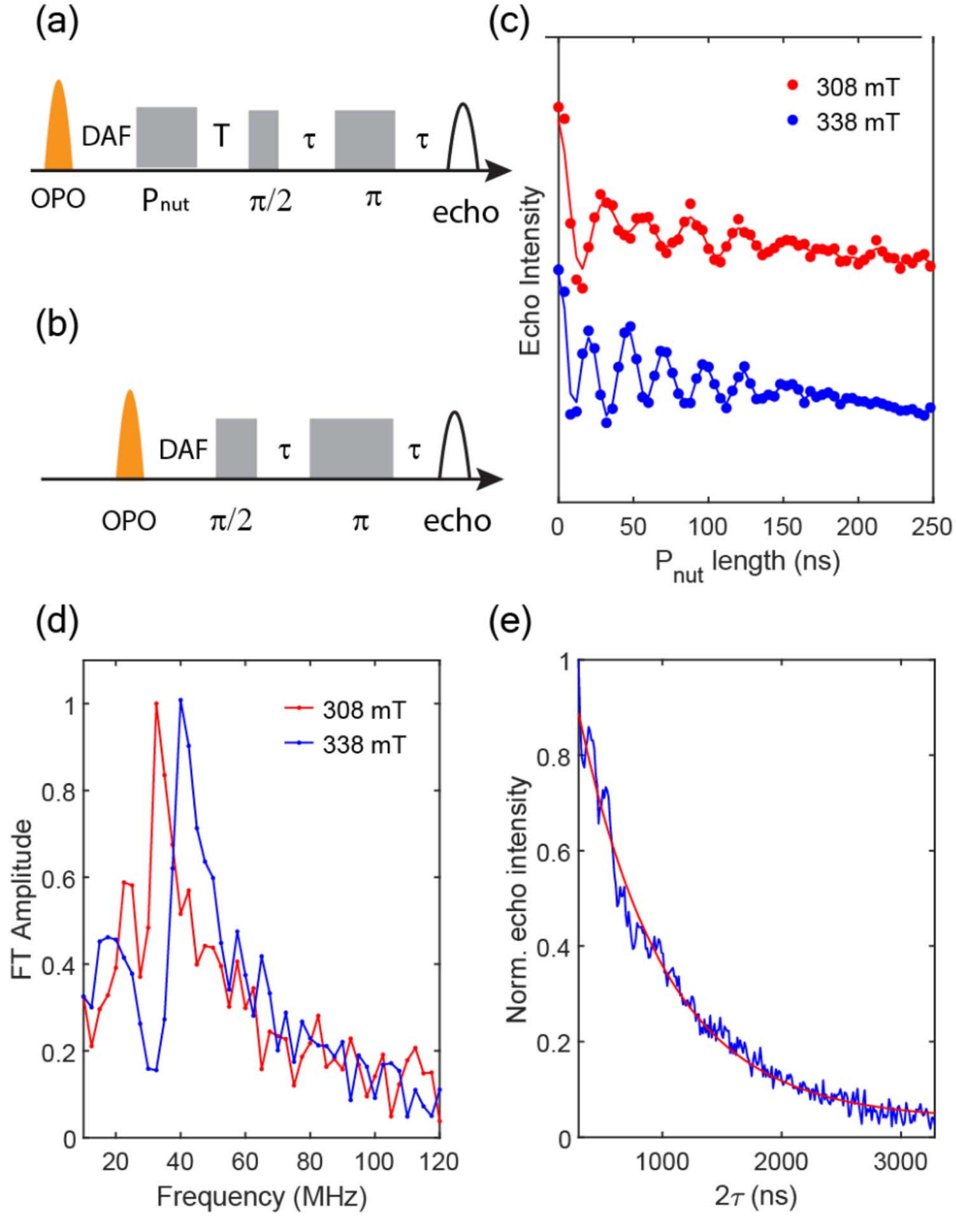

Fig. 6 (a) Pulse sequence for the transient nutation measurement, where T is 300 ns, τ is 148 ns, the $\pi/2$ pulse is 6 ns, π pulse is 12 ns, and the delay after flash (DAF) is $t_0 + \mathrm{d}t$, where $\mathrm{d}t = 30$ ns. (b) Pulse sequence for the T_2 measurement. (c) The nutation traces at 308 mT and 338 mT for **TPT** in 2-MeTHF at 10 K. (d) Fourier transformed data from (c). (e) Net spin magnetization decay trace at 338 mT for **TPT** in 2-MeTHF at 10 K using the pulse sequence in (b).

$m_s = \pm2$ and $m_s = \pm1$ in the ^{5}TT manifold. To rule out the possibility of aggregate induced EPR signals, we measure EPR spectra at 76 K for a concentrated solution of **PT** in 2-MeTHF (220 μM), and compare these to data collected for **TPT** under the same experimental conditions but at a lower (66 μM) concentration (Fig. S17a and b†). In Fig. S17a,† the ^{5}TT signal generated in **PT**/2-MeTHF can only arise from aggregation (because there is only one tetracene chromophore to harbor a triplet), and the EPR signal intensity is <10% of the **TPT**/2-MeTHF sample. In addition to the small intensity, the ^{5}TT spectral shape for **PT**/2-MeTHF is distinct from that of **TPT**/2-MeTHF. A factor of 6 reduction in the **TPT** concentration was also introduced and found to produce no significant perturbation to the EPR signals (Fig. S17c†). The lack of significant change to the steady-state absorption of **TPT** at low temperature (Fig. S17c†) further substantiates that the EPR signal in Fig. 5 originates from singlet fission of an ensemble of isolated **TPT** and contains little influence from aggregation.

To support our assignment for the EPR signal mentioned above, pulsed EPR experiments were conducted on **TPT** in 2-MeTHF at 10 K. Transient nutation traces were obtained with the pulse sequence shown in Fig. 6a at both 308 mT and 338 mT, and the data are shown in Fig. 6c. The Fourier transformed results (Fig. 6d) indicate extracted frequencies that are centered at 32.5 MHz and 40 MHz for the 308 mT and 338 mT nutation experiments, respectively. The ratio of these frequencies (0.81 : 1) is a close match to the ratio $\sqrt{2}\ :\ \sqrt{3}$ (*i.e.*, 0.816 : 1). Based on the equation $\omega_{\text{ms,ms}\pm1} = \frac{g\beta_e B_1}{\hbar}\sqrt{[S(S+1) - m_s(m_s+1)]}$, where B_1 is the microwave field strength and m_s represents spin quantum number, the EPR signal at 308 mT can be assigned to a transition between $m_s = \pm2$ and $m_s = \pm1$, while the signal at 338 mT is associated with the transition between $m_s = \pm1$ and $m_s = 0$, all within the ^{5}TT manifold.

To measure the spin dephasing lifetime (T_2), we operate on the spin states corresponding to the EPR signal at 338 mT with the Hahn echo pulse sequence shown in Fig. 6a. The transient net spin magnetization decay trace is displayed in Fig. 6d, obtained by modifying the relaxation time between the $\frac{\pi}{2}$ pulse, π pulse, and the echo. The decay trace is fit with a single exponential function leading to a determination of $T_2 = 726$ ns at 10 K.

Discussion

Despite evidence of some spectral shifts and transition dipole enhancement for the electronic transitions involving the pyrene bridge caused by interaction with the tetracenic chromophores, the overall picture still implicates weak coupling in the **TPT** dimer. Interaction between the tetracene and pyrene could be large, yet the coupling between the two tetracene chromophores through the pyrene bridge is relatively low based on the only weakly perturbed $S_1 \leftarrow S_0$ transition. Upon excitation from S_0 to S_1, TT is formed with a risetime of 4.5 ps at room temperature and 9.3 ps at 77 K. Due to the fast observed rate, internal conversion from S_1 to ^{1}TT is the most likely reaction pathway.[26] The temperature dependence suggests that singlet fission of **TPT** is a thermally activated process, which could in principle be an indication of a slightly endothermic energy balance between S_1 and ^{1}TT. However, the apparent equilibrium between S_1 and ^{1}TT, which has been observed in tetracenic systems,[20,25,27–29] strongly favors ^{1}TT in **TPT**, suggesting instead the overall reaction is exoergic. Because we observe no other species besides S_1 and ^{1}TT on the ns timescale, the equilibrium indicates that the singlet fission yield is about 94%, as the S_1 emission quantum yield is measured to be 6%. The singlet fission yield for pentacene dimers in most cases is close to 100%,[13,14,20,30–39] and is typically higher than tetracene dimers, which is lower than 50% in general.[16,20,40,41] For tetracene dimers bridged with a norbonyl ring studied by Gilligan *et al.*,[20] TIPS-BT1 and TIPS-BT1′, an equilibrium constant between S_1 and ^{1}TT was found to be 0.1 and 1, respectively. The small equilibrium constant of the tetracene dimers is due to the similar energetics of S_1 and ^{1}TT. On the other hand, the pentacene dimer, TIPS-BP1, has an equilibrium constant of 10^2–10^5 and the emission quantum yield is <0.01, indicating strong exothermicity from S_1 to ^{1}TT. From this perspective, **TPT** behaves closer to pentacene than tetracene, commensurate with its S_0–S_1 energy red-shift.

Given the slight exothermicity, the relatively fast fission rate for **TPT** compared with other weakly coupled tetracenes is not surprising. The rate falls below that of the fastest pentacene dimer systems with sub-ps singlet fission rates, and in those cases strong electronic coupling between chromophores can be implicated for accelerating the rate. In **TPT** however, the bridge does not evidently lead to strong chromophore–chromophore coupling, as judged by the unperturbed and only slightly shifted $S_1 \leftarrow S_0$ absorption bands. Only higher-lying absorption bands show evidence of mixed-state behavior involving charge redistribution, but these are not directly excited nor involved in singlet fission during our measurements. Nevertheless, models of singlet fission originally developed by Ratner, Michl, *et al.*[42] clearly show a role for virtual CT states in the SF process through the mediated mechanism. Modulating the importance of CT state involvement using solvent polarizability or polarity could be insightful, although here poor solubility in many solvents prevents a systematic study.

Now we turn to the eventual fate of ^{1}TT. From nsTA data, the decay lifetimes of ^{1}TT are 197 ns and 276 ns at 296 K and 77 K, respectively, indicating the decay of the ^{1}TT state is also a thermally activated process. One of the decay pathways for ^{1}TT is internal conversion to S_0, which can be seen from the dominant ground state bleach recovery on the ns timescale (Fig. 3d at 560 nm and Fig. S12d† at 568 nm, yellow traces). The other decay pathway could be from ^{1}TT to ^{5}TT, and we suggest here that nsTA data are consistent with the EPR data in this regard. In addition to the distinct ^{5}TT peak pattern with primary separation of $D/3$, the TREPR signals are further characterized to be from the pure ^{5}TT state using nutation frequencies from pulsed EPR at 10 K (Fig. 6). Importantly, these data lack any clear contribution from T_1. This then suggests that the longer-lived species identified in nsTA experiments – what was referred to earlier as species X – is due to ^{5}TT. Because we can now verify the long-lived species common to EPR and TA is ^{5}TT, we suggest that ^{5}TT has unique spectral features compared with ^{1}TT, which can be seen in Fig. S14a.† Distinct ESA features for ^{1}TT and ^{5}TT were also observed by Pace *et al.*[43] A more definitive method for connecting ^{5}TT photoinduced absorption and spin signatures involving optically detected magnetic resonance[44,45] is planned.

To gain a full kinetic picture, kinetic simulations are performed based on the scheme shown in Fig. 7. Comparison of the relative state populations as a function of time are shown in Fig. S21.† The long-lived ^{5}TT appears in nsTA throughout the temperature range with no obvious temperature dependence. For ^{1}TT, we assume that the competing pathways ($^1\text{TT} \rightarrow \text{S}_0$, $^1\text{TT} \rightarrow {}^5\text{TT}$) could both play some role in dictating the temperature dependence of TT deactivation. One possible mechanism for reduced $^1\text{TT} \rightarrow \text{S}_0$ decay at low temperature involves the constraint of the solvent environment that severely restricts the molecular motion of **TPT** upon freezing, decelerating relaxation from the ^{1}TT state to the S_0 state. The exact dynamics involved in the transition is unclear, as is the role that the aforementioned CT states might play, but the lower polarizability of the frozen solution may modulate their involvement. While $^1\text{TT} \rightarrow \text{S}_0$ is delayed as the solvent is gradually frozen to solid, $^1\text{TT} \rightarrow {}^5\text{TT}$ may also be slowed. The exact mechanism responsible here is again unknown, but it may be that large J fluctuations required to promote the transition[7] and caused by thermally induced motions are suppressed, reducing the observed rate of $^1\text{TT} \rightarrow {}^5\text{TT}$ population flow.

Despite the coincidence of long-lived signals assignable to ^{5}TT in TA and EPR, there is a lifetime mismatch between the long-living ESA from nsTA ($\tau > 35$ μs) and the ^{5}TT signal from TREPR that decays in ~3 μs. The EPR signal arises from spin polarization, proportional to the population difference between the magnetic spin states.[46] Consequently, the decay of the EPR signal does not signify the disappearance of population from the state, but instead the decrease of the population difference between the corresponding states. Namely, although the ^{5}TT signal from TREPR decays in ~3 μs due to spin-lattice relaxation, the ^{5}TT population lifetime can still be much longer. We fit the kinetic trace for TREPR spectra at 338 mT with a set of ordinary differential equations based on the scheme in Fig. S19c.† The normalized population for ^{1}TT and ^{5}TT states is shown in Fig. S19a.† The population difference between ^{5}TT(0) and ^{5}TT(1), representing the spin polarization between the two states, follows the kinetic trace for TREPR spectra at 338 mT, including the sign flipping at ~2500 ns. Furthermore, the fitted lifetimes of ^{1}TT and ^{5}TT roughly correlate with the lifetimes obtained from nsTA. From the ODE fit, τ_{11}, τ_{10}, τ_{SLR}, τ_1, and τ_0 are 106.6 ns, 446.3 ns, 2 μs, 19.1 μs, and 38.4 μs, respectively. From nsTA, $\tau_{1_{\text{TT}}}$ is 276 ns (similar to the average of τ_{11} and τ_{10}, the two ^{1}TT decay pathways), and $\tau_{5_{\text{TT}}}$ is >35 μs, consistent with the average of τ_1 and τ_0, the ^{5}TT decay pathways from different spin sublevels.

As for the EPR spectral shape of the ^{5}TT state, according to the literature,[7,12] it depends on the molecular geometry and the alignment between molecular axis and magnetic axis. For the organic dimers with the two chromophores aligned in parallel as in **TPT**, the population within the ^{5}TT state should be symmetric regarding $m_s = 0$, that is, $P(m_s = -1) = P(m_s = 1)$ and $P(m_s = -2) = P(m_s = 2)$, where P represents population. Because of the symmetric population distribution for the ^{5}TT manifold, the arrangement of features in the EPR spectrum should be approximately symmetric, accordingly. However, in Fig. 5, the spectrum throughout the magnetic field range is mostly positive and is asymmetric with respect to B_0 (334 mT). Absorptive spin polarization for ^{5}TT has been observed[10,14–16] and discussed in other systems. The transition from ^{1}TT to ^{5}TT is mediated by the fluctuation of exchange energy, in films or aggregates caused by triplet migration. This process is discussed by Kobori *et al.*[10,47]

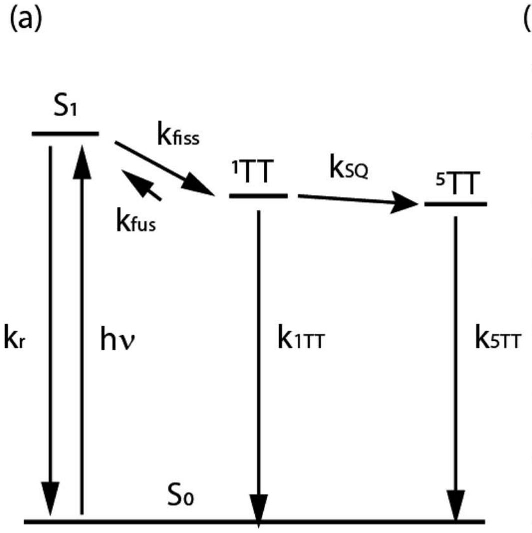

(b)

Unit : s^{-1}	RT	77K
kfiss	2.1 x 10^{11}	1.2 x 10^{11}
ΦEmi	6.5%	4.2 %
kfus	1.3 x 10^{10}	5.1 x 10^9
k1TT	4.7x 10^6	3.2 x 10^6
k5TT	< 2.9 x 10^4	< 2.9 x 10^4
kSQ	4.1 x 10^5	2.8 x 10^5

Fig. 7 (a) The kinetic scheme for **TPT** in 2-MeTHF upon excitation centered at 600 nm. (b) Resulting rate coefficients from a fit of the kinetic scheme to TA data. k_{fiss} was determined from fsTA data, and $k_{5\text{TT}}$ was given an upper bound based on estimated decay on a μs timescale. Φ_{emi} was fixed based on fluorescence quantum yield. k_{SQ} and $k_{1_{\text{TT}}}$ were varied in the fit of nsTA to match the ^{1}TT and ^{5}TT populations. Further details of the fit are in the ESI.†

in disordered TIPS-pentacene thin films and aggregated TIPS-pentacene solutions. In their chemically induced dynamic electron polarization (CIDEP) model, SQ_0 mixing takes place when the coupling of the triplet pair is weakened *via* triplet migration. Meanwhile, SQ_{-2} and SQ_{-1} become populated *via* level crossing at the corresponding distances between the triplet pair, and through zero-field splitting, population is trapped in $^5TT_0$, $^5TT_{-2}$, and $^5TT_{-1}$, resulting in absorptive spin polarization of ^5TT. No triplet migration is possible in **TPT**, nor are large-scale nuclear motions, so we disfavor this mechanism. Instead, we suggest that large and rare fluctuations in J produce ^5TT populations. We compare **TPT** behavior with predictions for planar but flexible pentacene dimers studied by MacDonald *et al.*,[48] who interpret net-absorptive quintet peaks in CW EPR and symmetric ^5TT spectra in pulsed-EPR to arise from SQ-mixing (*i.e.*, low J, fast decoherence)[49] and stochastic processes (high J, slower decoherence),[50] respectively. These regimes may be simultaneously available in their ensemble due to conformational flexibility, absent in **TPT**. The fact that cw-EPR and echo-detected X-band spectra for **TPT** roughly match (Fig. 5b and S20a,† both are net-absorptive with similar shapes), confirms that quintets are not likely forming *via* low-J SQ mixing because such net-absorptive quintets should be strongly suppressed by the echo detection process. Therefore, net-absorptive X-band spectra seemingly arise in the stochastic regime due to asymmetrically-populated quintets not subject to fast decoherence, whereas the population becomes more symmetric at Q-band (Fig. S20b†). This type of field-dependent mechanism requires further theoretical investigation, and we note that the full collection of cw- and pulsed-EPR at different field strengths are needed to develop a complete picture.[51]

One of the primary goals for QIS applications with the ^5TT state is to increase the dephasing time, T_2, and the population of purely spin-polarized ^5TT sublevels. In this study, abundant ^5TT is produced such that the ^5TT state can be monitored by both nsTA and EPR. Higher ^5TT yield has been reported in monomer thin films[8–10,43,51] or weakly coupled dimers,[13–16,18,19] but it inevitably comes with isolated T_1 because the interchromophore interaction can become weak enough to enable the spin mixing and decorrelation process to T_1.[14,19] The ^1TT decay pathways for these cases are proposed to be $^1TT \rightarrow {}^5TT \rightleftharpoons T_1 + T_1$ or through intersystem crossing from ^5TT to ^3TT, generating T_1 in two steps. However, **TPT** is an example of a weakly coupled dimer from the pure electronic coupling standpoint (and as judged by steady-state spectroscopy), where there is no evidence for isolated triplets generated through ^5TT. The features that could give rise to this behavior are the rigid bridge, the co-planar orientation, and the near-resonance of mixed chromophore-bridge electronic states. The outcome of these characteristics is an unusually large J at the equilibrium geometry, which is one of the keys to generate spin-polarized ^5TT without coexistence of T_1, stated in the parallel JDE model.[7] For the weakly coupled dimers and the monomer thin films that generate T_1, J is estimated to be <100 GHz,[10,13,15,16,43,51] and sometimes close to 0 GHz, indicating the energies of ^1TT, ^5TT and $2{*}T_1$ are about the same. For **TPT**, from broken symmetry DFT calculation as described in detail in the ESI,† J is calculated to be −512 GHz, where the absolute value is higher than the weakly coupled chromophores mentioned above, and the negative sign suggests ^5TT to be lower in energy than ^1TT. We thus hypothesize that the exchange energy of **TPT** is strong enough to slow the formation of uncorrelated T_1, given that there are limited intramolecular degrees of freedom available to promote the $^5TT \rightarrow (T_1 + T_1)$ transition, unlike dimers with flexible bridges.

The dephasing time, T_2, of the ^5TT manifolds is measured to be 726 ns, and it is long enough for us to demonstrate more than 4 Rabi oscillating cycles with the pulsed microwave setting mentioned previously. At 338 mT, for example, the EPR signal corresponds to the transition between $m_s = 0$ and $m_s = 1$ in ^5TT, and with pulsed microwaves, we can rotate the population between the two magnetic spin states, therefore demonstrating this two-level system as a qubit.

Conclusion

We design a parallel pyrene-bridged tetracene dimer, TPT, with coupled triplet spins for purposes of demonstrating pure spin polarization production relevant to QIS applications. Excited states are calculated to involve both tetracene and pyrene, yet the lowest singlet transitions are only weakly perturbed from the **PT** to **TPT**, suggesting minimal interchromophore communication across the bridge. The interaction between tetracene chromophores is optimized to allow the singlet-quintet mixing and trap the population in the ^5TT state while preventing the production of T_1. We have observed ^5TT with optical transient absorption spectra, which is rarely reported, through kinetic and temperature-dependent measurements that correlate with observations of ^5TT using EPR. We characterize the qubits in ^5TT manifolds with TREPR and pulsed EPR, and the dephasing time approaches the μs timescale. The pure ^5TT state produced in large population is a highlight of this work; however, to generate high-quality qubits for QIS applications, we not only need a large population solely in the ^5TT state, but also pure spin-polarized ^5TT state. Toward this end, we suggest aiming future efforts to align all **TPT** dimers with their principal magnetic axis along an applied magnetic field direction.

Data availability

Crystallographic data for **TPT** has been deposited at the Cambridge Structural Database under deposition number 2299672. TDDFT log files have been uploaded as part of the ESI.†

Author contributions

LL performed all spectroscopic experiments and analysis, supervised by JCJ and NHD, and wrote the experimental portions of the manuscript. JCJ assisted with spectroscopic experiments and advised on the data analysis and manuscript writing with NHD. JEA designed the target molecules and the experimental approach, and JEA and TS devised the appropriate chromophores for singlet fission studies. TS performed and optimized the synthesis and conducted appropriate structural characterization. QA contributed conceptualization and investigation of calculation methodology and wrote portions of the manuscript. CR supervised and conceptualized computational efforts and contributed to reviewing and editing the manuscript.

Conflicts of interest

There are no conflicts to declare.

Acknowledgements

Work on transient absorption and time-resolved electron paramagnetic resonance spectroscopy was supported by the Solar Photochemistry Program of the U.S. Department of Energy, Office of Basic Energy Sciences, Division of Chemical Sciences, Biosciences, and Geosciences. We acknowledge funding for steady-state spectroscopy and aggregation studies from the National Science Foundation (CHE-2102713). Q. A. and C. R. acknowledge funding from the National Science Foundation through the Designing Materials to Revolutionize and Engineer our Future (NSF DMREF) program under award number DMR 1627428, and thank the University of Kentucky Center for Computational Sciences and Information Technology Services Research Computing for their fantastic support and collaboration and use of the Lipscomb Compute Cluster and associated research computing resources. We thank Sean Parkin, University of Kentucky X-ray crystallography facility, for obtaining the **TPT** crystal structure. This work was authored by Alliance for Sustainable Energy, Limited Liability Company, the manager and operator of the National Renewable Energy Laboratory under Contract No. DE-AC36-08GO28308. The views expressed in the article do not necessarily represent the views of the Department of Energy or the U.S. Government. The U.S. Government retains and the publisher, by accepting the article for publication, acknowledges that the U.S. Government retains a nonexclusive, paid-up, irrevocable, worldwide license to publish or reproduce the published form of this work, or allow others to do so, for U.S. Government purposes.

References

1 M. J. Y. Tayebjee, D. R. McCamey and T. W. Schmidt, Beyond Shockley–Queisser: Molecular Approaches to High-Efficiency Photovoltaics, *J. Phys. Chem. Lett.*, 2015, **6**, 2367–2378.

2 M. B. Smith and J. Michl, Recent Advances in Singlet Fission, *Annu. Rev. Phys. Chem.*, 2013, **64**, 361–386.

3 M. B. Smith and J. Michl, Singlet Fission, *Chem. Rev.*, 2010, **110**, 6891–6936.

4 M. C. Hanna and A. J. Nozik, Solar conversion efficiency of photovoltaic and photoelectrolysis cells with carrier multiplication absorbers, *J. Appl. Phys.*, 2006, **100**, 074510.

5 M. J. Y. Tayebjee, A. A. Gray-Weale and T. W. Schmidt, Thermodynamic Limit of Exciton Fission Solar Cell Efficiency, *J. Phys. Chem. Lett.*, 2012, **3**, 2749–2754.

6 I. Paci, et al., Singlet Fission for Dye-Sensitized Solar Cells: Can a Suitable Sensitizer Be Found?, *J. Am. Chem. Soc.*, 2006, **128**, 16546–16553.

7 K. E. Smyser and J. D. Eaves, Singlet fission for quantum information and quantum computing: the parallel JDE model, *Sci. Rep.*, 2020, **10**, 18480.

8 D. Lubert-Perquel, et al., Identifying triplet pathways in dilute pentacene films, *Nat. Commun.*, 2018, **9**, 4222.

9 R. D. Pensack, et al., Observation of Two Triplet-Pair Intermediates in Singlet Exciton Fission, *J. Phys. Chem. Lett.*, 2016, **7**, 2370–2375.

10 H. Nagashima, et al., Singlet-Fission-Born Quintet State: Sublevel Selections and Trapping by Multiexciton Thermodynamics, *J. Phys. Chem. Lett.*, 2018, **9**, 5855–5861.

11 L. R. Weiss, et al., Strongly exchange-coupled triplet pairs in an organic semiconductor, *Nat. Phys.*, 2017, **13**, 176–181.

12 R. D. Dill, K. E. Smyser, N. H. Damrauer and J. D. Eaves Entangled, Spin-polarized Excitons from Singlet Fission in a Rigid Dimer, *Nat. Commun.*, 2023, **14**, 1180.

13 M. J. Y. Tayebjee, et al., Quintet multiexciton dynamics in singlet fission, *Nat. Phys.*, 2017, **13**, 182–188.

14 B. S. Basel, et al., Unified model for singlet fission within a non-conjugated covalent pentacene dimer, *Nat. Commun.*, 2017, **8**, 15171.

15 S. Nakamura, et al., Synergetic Role of Conformational Flexibility and Electronic Coupling for Quantitative Intramolecular Singlet Fission, *J. Phys. Chem. C*, 2021, **125**, 18287–18296.

16 Y. Matsui, et al., Exergonic Intramolecular Singlet Fission of an Adamantane-Linked Tetracene Dyad via Twin Quintet Multiexcitons, *J. Phys. Chem. C*, 2019, **123**, 18813–18823.

17 Q. Ai, et al., Nanoribbons or weakly connected acenes? The influence of pyrene insertion on linearly extended ring systems, *J. Mater. Chem. C*, 2021, **9**, 16929–16934.

18 B. S. Basel, et al., Evidence for Charge-Transfer Mediation in the Primary Events of Singlet Fission in a Weakly Coupled Pentacene Dimer, *Chem*, 2018, **4**, 1092–1111.

19 A. B. Pun, et al., Ultra-fast intramolecular singlet fission to persistent multiexcitons by molecular design, *Nat. Chem.*, 2019, **11**, 821–828.

20 A. T. Gilligan, E. G. Miller, T. Sammakia and N. H. Damrauer, Using Structurally Well-Defined Norbornyl-Bridged Acene Dimers to Map a Mechanistic Landscape for Correlated Triplet Formation in Singlet Fission, *J. Am. Chem. Soc.*, 2019, **141**, 5961–5971.

21 J. D. Cook, T. J. Carey and N. H. Damrauer, Solution-Phase Singlet Fission in a Structurally Well-Defined Norbornyl-Bridged Tetracene Dimer, *J. Phys. Chem. A*, 2016, **120**, 4473–4481.

22 H. Du, R. A. Fuh, J. Li, L. A. Corkan and J. S. Lindsey, PhotochemCAD++: A Computer-Aided Design and Research Tool in Photochemsitry, *Photochem. Photobiol.*, 1998, **62**, 141–142.

23 H. F. Bettinger, C. Tönshoff, M. Doerr and E. Sanchez-Garcia, Electronically Excited States of Higher Acenes up to Nonacene: A Density Functional Theory/Multireference

Configuration Interaction Study, *J. Chem. Theory Comput.*, 2016, **12**, 305–312.

24 J. C. Dean, et al., Photophysical characterization and time-resolved spectroscopy of a anthradithiophene dimer: exploring the role of conformation in singlet fission, *Phys. Chem. Chem. Phys.*, 2017, **19**, 23162–23175.

25 K. Miyata, et al., Coherent singlet fission activated by symmetry breaking, *Nat. Chem.*, 2017, **9**, 983–989.

26 N. V. Korovina, N. F. Pompetti and J. C. Johnson, Lessons from intramolecular singlet fission with covalently bound chromophores, *J. Chem. Phys.*, 2020, **152**, 040904.

27 N. R. Monahan, et al., Dynamics of the triplet-pair state reveals the likely coexistence of coherent and incoherent singlet fission in crystalline hexacene, *Nat. Chem.*, 2017, **9**, 341–346.

28 K. Miyata, F. S. Conrad-Burton, F. L. Geyer and X.-Y. Zhu, Triplet Pair States in Singlet Fission, *Chem. Rev.*, 2019, **119**, 4261–4292.

29 M. W. B. Wilson, et al., Temperature-Independent Singlet Exciton Fission in Tetracene, *J. Am. Chem. Soc.*, 2013, **135**, 16680–16688.

30 J. Zirzlmeier, et al., Singlet fission in pentacene dimers, *Proc. Natl. Acad. Sci. U. S. A.*, 2015, **112**, 5325–5330.

31 C. Hetzer, et al., Chromophore Multiplication To Enable Exciton Delocalization and Triplet Diffusion Following Singlet Fission in Tetrameric Pentacene, *Angew. Chem., Int. Ed.*, 2019, **58**, 15263–15267.

32 J. Zirzlmeier, et al., Solution-based intramolecular singlet fission in cross-conjugated pentacene dimers, *Nanoscale*, 2016, **8**, 10113–10123.

33 S. N. Sanders, et al., Quantitative Intramolecular Singlet Fission in Bipentacenes, *J. Am. Chem. Soc.*, 2015, **137**, 8965–8972.

34 K. C. Krishnapriya, et al., Spin density encodes intramolecular singlet exciton fission in pentacene dimers, *Nat. Commun.*, 2019, **10**, 33.

35 H. Sakai, et al., Multiexciton Dynamics Depending on Intramolecular Orientations in Pentacene Dimers: Recombination and Dissociation of Correlated Triplet Pairs, *J. Phys. Chem. Lett.*, 2018, **9**, 3354–3360.

36 T. Sakuma, et al., Long-Lived Triplet Excited States of Bent-Shaped Pentacene Dimers by Intramolecular Singlet Fission, *J. Phys. Chem. A*, 2016, **120**, 1867–1875.

37 E. Kumarasamy, et al., Tuning Singlet Fission in π-Bridge-π Chromophores, *J. Am. Chem. Soc.*, 2017, **139**, 12488–12494.

38 T. Yamakado, Conformational planarization *vs.* singlet fission: Distinct excited-state dynamics of cyclooctatetraene-fused acene dimers, *Angew. Chem., Int. Ed.*, 2018, **57**, 5438.

39 S. Lukman, et al., Tuneable Singlet Exciton Fission and Triplet–Triplet Annihilation in an Orthogonal Pentacene Dimer, *Adv. Funct. Mater.*, 2015, **25**, 5452–5461.

40 A. M. Müller, Y. S. Avlasevich, K. Müllen and C. J. Bardeen, Evidence for exciton fission and fusion in a covalently linked tetracene dimer, *Chem. Phys. Lett.*, 2006, **421**, 518–522.

41 N. V. Korovina, et al., Linker-Dependent Singlet Fission in Tetracene Dimers, *J. Am. Chem. Soc.*, 2018, **140**, 10179–10190.

42 E. C. Greyson, J. Vura-Weis, J. Michl and M. A. Ratner, Maximizing Singlet Fission in Organic Dimers: Theoretical Investigation of Triplet Yield in the Regime of Localized Excitation and Fast Coherent Electron Transfer, *J. Phys. Chem. B*, 2010, **114**, 14168–14177.

43 N. A. Pace, et al., Conversion between triplet pair states is controlled by molecular coupling in pentadithiophene thin films, *Chem. Sci.*, 2020, **11**, 7226–7238.

44 G. Joshi, et al., Optical readout of singlet fission biexcitons in a heteroacene with photoluminescence detected magnetic resonance, *J. Chem. Phys.*, 2022, **157**, 164702.

45 R. D. Dill, et al., Near-Infrared Absorption Features of Triplet-Pair States Assigned by Photoinduced-Absorption-Detected Magnetic Resonance, *J. Phys. Chem. Lett.*, 2023, **14**, 2387–2394.

46 C. Hintze, U. E. Steiner and M. Drescher, Photoexcited Triplet State Kinetics Studied by Electron Paramagnetic Resonance Spectroscopy, *ChemPhysChem*, 2017, **18**, 6–16.

47 S. Matsuda, S. Oyama and Y. Kobori, Electron spin polarization generated by transport of singlet and quintet multiexcitons to spin-correlated triplet pairs during singlet fissions, *Chem. Sci.*, 2020, **11**, 2934–2942.

48 T. S. C. MacDonald, M. J. Y. Tayebjee, M. I. Collins, E. Kumarasamy, S. N. Sanders, M. Y. Sfeir, L. M. Campos and D. R. McCamey, Anisotropic Multiexciton Quintet and Triplet Dynamics in Singlet Fission *via* Pulsed Electron Spin Resonance, *J. Am. Chem. Soc.*, 2023, **145**(28), 15275–15283.

49 M. I. Collins, M. R. McCamey and M. J. Y. Tayebjee, Fluctuating exchange interactions enable quintet multiexciton formation in singlet fission, *J. Chem. Phys.*, 2019, **151**, 164104.

50 M. I. Collins, F. Campaioli, M. J. Y. Tayebjee, J. H. Cole and D. R. McCamey, Quintet formation, exchange fluctuations, and the role of stochastic resonance in singlet fission, *Commun. Phys.*, 2023, **6**, 65.

51 B. K. Rugg, *et al.*, Triplet-pair spin signatures from macroscopically aligned heteroacenes in an oriented single crystal, *Proc. Natl. Acad. Sci. U. S. A.*, 2022, **119**, e2201879119.